

# Effect of Microstructures on Fatigue Crack Growth Behavior of Friction Stir Processed NiAl Bronze Alloy



YUTING LV, YANG DING, YUANFEI HAN, LAIZHI WU, LIQIANG WANG,  
and WEIJIE LU

Friction stir processed (FSPed) NAB alloy exhibits inhomogeneous microstructures that can be divided into three subregions from the top surface to the bottom according to  $\alpha$  phase morphologies: Widmanstätten  $\alpha$  subregion, banded  $\alpha$  colonies, and stream-like  $\alpha$  colonies. In this study, a constant stress intensity range ( $\Delta K$ ) was used for each sample to study the effect of microstructures on the fatigue crack growth rate (FCGR) of FSPed NAB alloy. The results show that  $\alpha$  phase in banded and stream-like  $\alpha$  colonies experiences completely dynamic recrystallization and forms equiaxed  $\alpha$  grains during FSP. The FCGR of FSPed NAB alloy continuously decreases from the top surface to the bottom. In the subregion with stream-like  $\alpha$  colonies, the alloy containing a higher content of equiaxed  $\alpha$  grains and fine  $\kappa_{iv}$  phase, and less retained  $\beta$  ( $\beta'$ ) phase exhibits the best FCG resistance. The equiaxed  $\alpha$  grains deflect the main crack and increase crack tortuosity effect, which make a main contribution to FCG resistance of FSPed NAB alloy, while martensite  $\beta'$  phase produced during FSP accelerates its fatigue crack growth. Compared to matrix alloy, FSPed NAB alloy exhibits better FCG resistance only at high  $\Delta K$  levels. At low  $\Delta K$  levels, the crack deflection effect caused by coarser  $\kappa$  phase in the matrix alloy obviously improves its FCG resistance. With the increasing  $\Delta K$ , the aforementioned crack deflection effect gradually diminishes and fatigue crack prefers to propagate in a flat way, resulting in higher FCGR of matrix alloy.

DOI: 10.1007/s11661-016-3937-1

© The Minerals, Metals & Materials Society and ASM International 2017

## I. INTRODUCTION

NICKEL-ALUMINUM bronze (NAB) alloy is widely used in marine engineering materials of propeller, pump, valve, *etc.* due to its excellent combination of high strength and corrosion resistance.<sup>[1]</sup> With the development of ocean engineering around the world, NAB alloy has been paid more and more attention by many material scientists.<sup>[1–3]</sup> Typical microstructures of the as-cast NAB include  $\alpha$  phase, retained  $\beta$  ( $\beta'$ ) phase, and several precipitation phases ( $\kappa_i$ ,  $\kappa_{ii}$ ,  $\kappa_{iii}$ , and  $\kappa_{iv}$ ).<sup>[4]</sup> The complex microstructures are disadvantageous to the mechanical properties and corrosion resistance of the as-cast NAB alloy.<sup>[5]</sup> For example, Xu *et al.* reported that high interphase stress was formed between  $\alpha$  matrix

and  $\kappa$  phases when NAB alloy was deformed in elastic–plastic region (about 300–450 MPa). Fracture might initiate from the  $\alpha/\kappa$  phase boundaries due to the high interphase stress.<sup>[6]</sup> Fonlupt *et al.* found that NAB alloy containing more second phases had higher stress corrosion cracking susceptibility.<sup>[7]</sup> In addition, porosity defects are also formed due to gas evolution during solidification and fatigue crack can initiate and propagate from these defects, which are also adverse to the mechanical properties of NAB alloy.<sup>[8,9]</sup>

Recently, several techniques have been adopted to improve the mechanical properties and corrosion resistance of the as-cast NAB alloy such as ion implantation,<sup>[10]</sup> laser surface melting,<sup>[11,12]</sup> friction stir processing (FSP),<sup>[13,14]</sup> and friction surfacing (FS).<sup>[15]</sup> Among them, FSP has been rapidly developed due to its energy efficiency, environmental friendliness, and versatility.<sup>[16]</sup> Although this technique is originally intended for aluminum alloys, the applications have now been extended to various alloys such as magnesium, copper, titanium, and steels.<sup>[16]</sup> One important advantage is that only the component surface is modified, while for NAB component used in ocean engineering almost all the damages occur on the surface. Thus, FSP is a suitable technique to make uniform the surface microstructures of the as-cast NAB alloy and to improve its mechanical properties and corrosion resistance.<sup>[17]</sup>

Previous investigations showed that FSP refined the microstructures and eliminated the porosity defects of the as-cast NAB alloy, thus improving its mechanical

YUTING LV is with the State Key Laboratory of Metal Matrix Composites, Shanghai Jiao Tong University, Shanghai 200240, P.R. China, and also with the Collaborative Innovation Center for Advanced Ship and Deep-Sea Exploration, Shanghai 200240, P.R. China. YANG DING and YUANFEI HAN are with the State Key Laboratory of Metal Matrix Composites, Shanghai Jiao Tong University. LAIZHI WU is with the Jiujiang Branch of 707 Institute of China Shipbuilding Industry Corporation, Jiujiang 332007, P.R. China. LIQIANG WANG and WEIJIE LU are with the State Key Laboratory of Metal Matrix Composites, Shanghai Jiao Tong University, and also with the Collaborative Innovation Center for Advanced Ship and Deep-Sea Exploration, No. 800 Dongchuan Road, Materials Science and Engineering Building D329, Minhang District, Shanghai, 200240, P.R. China. Contact emails: luweijie@sjtu.edu.cn, wang\_liqiang@sjtu.edu.cn

Manuscript submitted October 13, 2016.

Article published online January 13, 2017

properties and corrosion resistance significantly.<sup>[14,18]</sup> However, inhomogeneous microstructures were also formed during FSP, which included fine Widmanstatten structure, banded structure, equiaxed structure, stream-like structure, and onion ring structure.<sup>[14,19]</sup> This is because various regions in the Friction stir processed (FSPed) NAB alloy experience different thermomechanical histories.<sup>[19]</sup> The peak temperature of stir zone can reach 1263 K to 1288 K (990 °C to 1015 °C) at which temperature the NAB alloy is entirely in  $\beta$  phase zone and Widmanstatten  $\alpha$  structure is formed after FSP due to high cooling rate.<sup>[20]</sup> The banded  $\alpha$  structure results from incomplete dynamic recrystallization and intense plastic deformation of FSP,<sup>[19]</sup> while the onion ring structure is formed due to severe plastic deformation at higher rotation rate and traverse speed.<sup>[2]</sup> The inhomogeneous microstructures produced during FSP depend on material properties, tool geometry features, and processing parameters.<sup>[21]</sup> Increasing the number of FSP passes can produce more homogeneous structures in the stir zone, but it cannot eliminate the inhomogeneous structures completely.<sup>[19]</sup>

For structural materials, fatigue crack growth rate (FCGR) is an important parameter for their engineering applications. Thus, it is necessary to understand the FCGR of FSPed NAB alloy. However, to our knowledge, FCGR of FSPed NAB alloy has rarely been studied. In addition, inhomogeneous microstructures formed during FSP result in different FCGRs at various subregions,<sup>[19]</sup> and it is difficult to estimate which microstructures exhibit the best fatigue crack growth resistance. Therefore, in this study, FSP is used to process the NAB alloy and to form inhomogeneous microstructures from the top surface to the bottom. Then a constant stress intensity range ( $\Delta K$ ) is used for each sample to study the effect of microstructures on the FCGR of FSPed NAB alloy. In order to study the FCGR of various subregions as a function of  $\Delta K$ , we chose four  $\Delta K$  values, *i.e.*, 7, 7.7, 8.4, and 9.8 MPa $\sqrt{\text{m}}$ , to test the FCGR of FSPed NAB alloy.

## II. EXPERIMENTAL PROCEDURE

The as-cast Cu-9.5Al-4.2Ni-4Fe-1.2Mn NAB alloy ingot with a dimension of  $\phi 150 \text{ mm} \times 100 \text{ mm}$  was prepared by vacuum melting and then forged at 1123 K (850 °C). The microstructures of the forged alloy mainly consist of  $\alpha$  matrix, coarser  $\kappa_{\text{ii}}$ , finer  $\kappa_{\text{iv}}$ , and  $\beta'$  phases,<sup>[22]</sup> as shown in Figures 1(a) and (b). The NAB alloy was subjected to FSP at a traverse speed of 100 mm/minute and a rotation rate of 1000 rpm. The FSP tool used in this study is a tungsten carbide-based alloy with a shoulder of 15 mm diameter and an unthreaded pin of 7 mm diameter and 2 mm height. The FSPed NAB alloy exhibits inhomogeneous microstructures from the top surface to the bottom. According to the primary microstructures of various subregions, the stir zone of FSPed NAB alloy can be divided into three subregions, which are named as subregion A, B, and C, respectively. The three subregions correspond to locations 0–1.1 mm, 1.1–1.6 mm,

and 1.6–2.1 mm, respectively, from the top surface of FSPed NAB alloy, as shown in Figure 2.

Three-point bending specimens were cut from an FSPed NAB plate using a wire cutting machine. Schematic drawing of the extraction of three-point bending specimens from the FSPed NAB plate is shown in Figure 3(a). As can be seen, the notch used in this study is located in the middle of the top surface along the advancing direction of FSPed NAB alloy. Figure 3(b) shows the major dimensions of test specimens machined in accordance with ASTM E399 standards. In order to guide the crack growth straight along the perpendicular direction and obtain more accurate results, side grooves were machined. Therefore, in this study, the effective specimen thickness ( $B_{\text{eff}}$ ) was used to calculate the stress intensity factor ( $K$ ). According to ASTM E399,  $B_{\text{eff}} = \sqrt{B * B_N}$ , where  $B$  is the specimen thickness and  $B_N$  is the specimen thickness between the roots of the side grooves.

FCGR tests were performed on a DLU-50 test machine from Bairuo and direct current potential drop (DCPD) method was used to determine the crack length of FSPed NAB alloy. Before the FCGR test, a fatigue pre-crack of about 0.3 mm was produced on the specimens using a load ratio  $R$  ( $K_{\text{min}}/K_{\text{max}}$ ) of 0.3 and a frequency of 1 Hz. In order to investigate the effect of microstructures on the FCGR of FSPed NAB alloy, a constant maximum stress intensity factor ( $K_{\text{max}}$ ) was used for each sample and the FCGR of different subregions was calculated using Origin software according to the tested crack length curve. Four  $K_{\text{max}}$  values, *i.e.*, 10, 11, 12, and 14 MPa $\sqrt{\text{m}}$ , were chosen to test FCGR variations as a function of  $K_{\text{max}}$ . The stress intensity range ( $\Delta K$ ) can be calculated using the formula:  $\Delta K = K_{\text{max}} * (1 - R)$ , where  $R$  is the load ratio. Therefore, the values of  $\Delta K$  used in this study are 7, 7.7, 8.4, and 9.8 MPa $\sqrt{\text{m}}$ .

The microstructural and crack morphology observations of FSPed NAB alloy were carried out using an optical microscope (OM) and a JEM-2100F scanning electron microscope (SEM) equipped with electron backscatter diffraction (EBSD). The sample preparation methods for SEM and EBSD observations have been described in detail in our previous investigations.<sup>[22–24]</sup> Vickers microhardness was measured on the polished cross-section using an automated tester with a load of 500 g and a dwelling time of 15 seconds. Each value was averaged from four tests.

## III. EXPERIMENTAL RESULTS

### A. Microstructures

Figure 4 shows the microstructures of subregions A, B, and C in the FSPed NAB alloy. In subregion A, the microstructures consist of Widmanstatten  $\alpha$  and  $\beta'$  phases (Figure 4(a)), subregion B shows similar microstructures but  $\alpha$  colonies exhibits a banded morphology. At the bottom of the stir zone, *i.e.*, subregion C, stream-like  $\alpha$  colonies and  $\beta'$  phase are observed (Figure 4(e)). The direction of the stream-like  $\alpha$  colonies is parallel to the rotation direction of FSP tool tip.



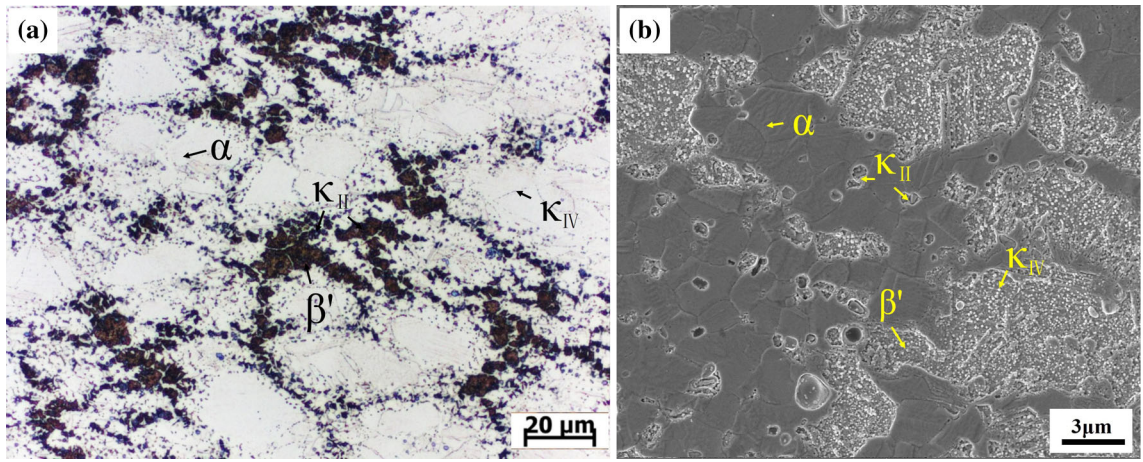


Fig. 1—Initial microstructures of forged NAB alloy: (a) OM image and (b) SEM image.

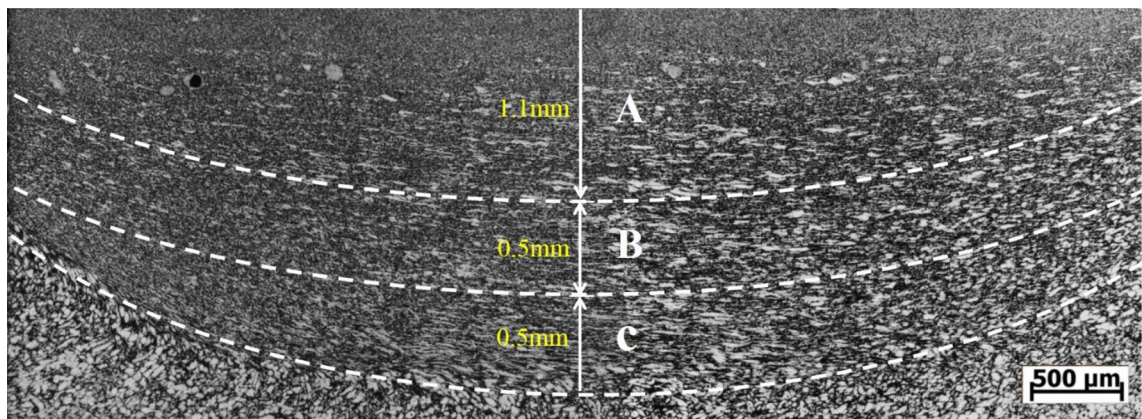


Fig. 2—Cross-section macrostructures of FSPed NAB alloy.

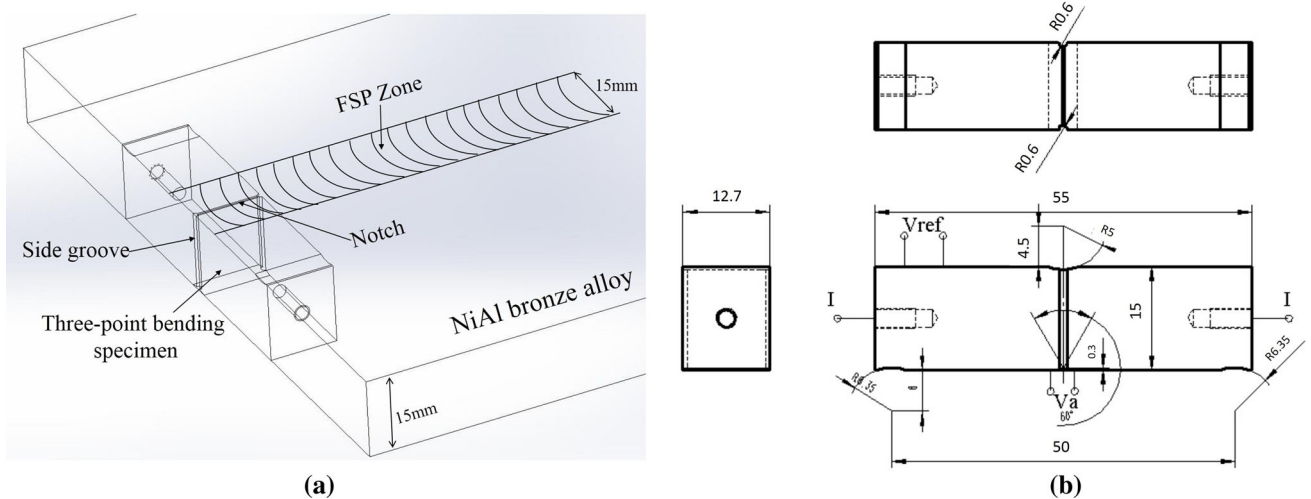


Fig. 3—(a) Schematic drawing of the extraction of three-point bending specimens from FSPed NiAl bronze plate. (b) The dimensions of samples for fatigue crack growth rate test.

Magnified images of subregions A, B, and C clearly reveal that fine  $\kappa_{IV}$  phase is also formed during FSP (Figures 4(b), (d), and (f)). It is worth mentioning that subregion B contains the most  $\kappa_{IV}$  phase among the three

subregions, while subregion C contains some coarser  $\kappa_{II}$  phase. The above results indicate that various subregions in the FSPed NAB alloy experience different thermomechanical histories, thereby producing



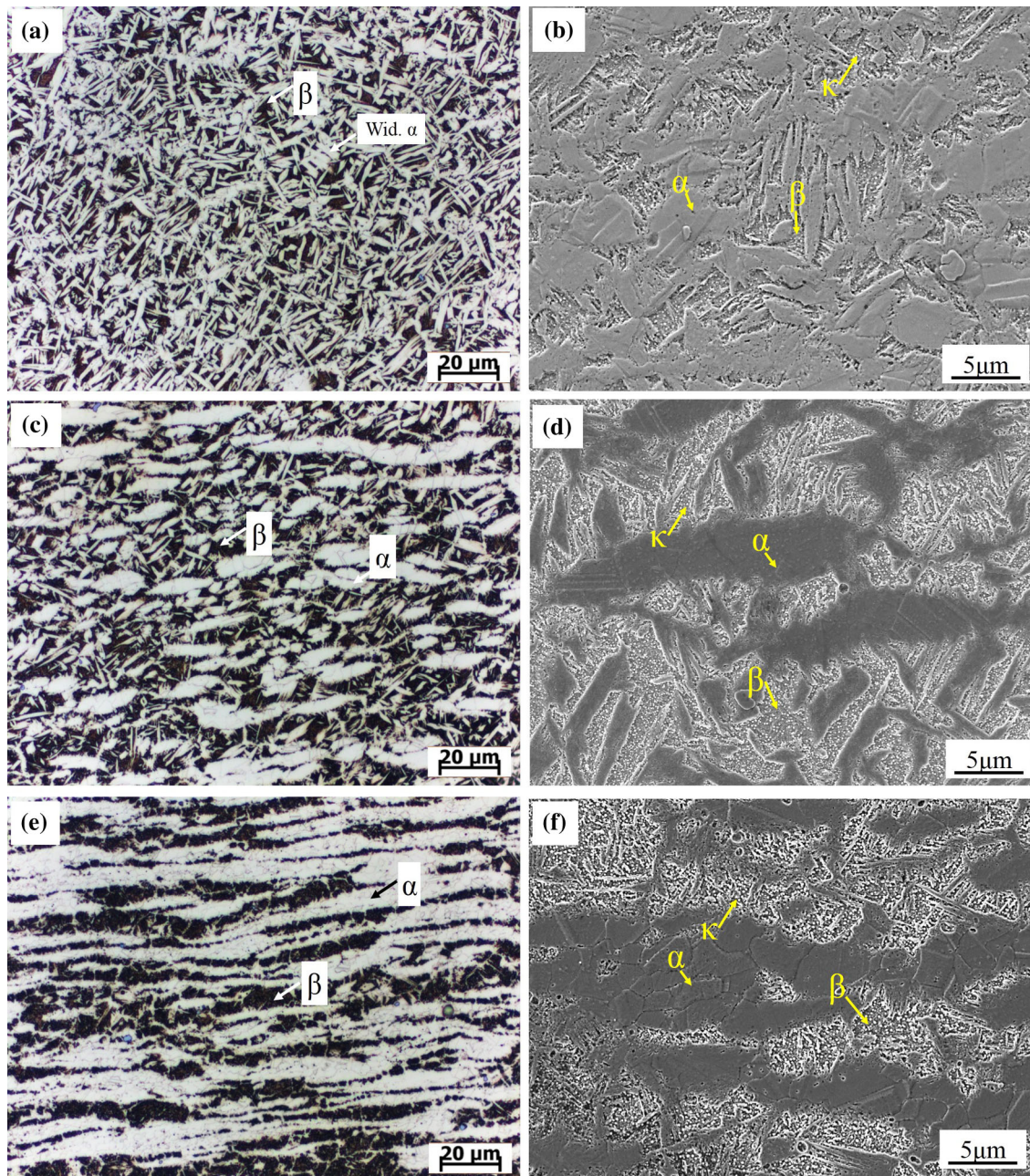


Fig. 4—OM and SEM images showing inhomogeneous microstructures in different zones of FSPed NAB alloy. (a), (c), and (e) Locations A, B, and C, respectively, in Fig. 2. (b), (d), and (f) Magnified images in (a), (c), and (e), respectively.

inhomogeneous microstructures from the top surface to the bottom.

### B. Fatigue Crack Growth Rate of FSPed NAB Alloy

Figure 5 shows the FCGRs of FSPed NAB alloy tested at the stress intensity values of 7, 7.7, 8.4, and 9.8  $\text{MPa}\sqrt{\text{m}}$ , respectively. As can be seen,  $\Delta K$  plays an important role in FCGR of FSPed NAB alloy (Figure 5(a)). The FCGRs of various subregions calculated from time vs crack length curves (Figure 5(a)) are shown in Figure 5 (b). The results clearly show that the FCGR decreases gradually from the top surface to the

matrix at the  $\Delta K$  values of 7 and 7.7  $\text{MPa}\sqrt{\text{m}}$ . While at the  $\Delta K$  values of 8.4 and 9.8  $\text{MPa}\sqrt{\text{m}}$ , the lowest FCGR is obtained at the distance of around 2 mm from the top surface, *i.e.*, subregion C in FSPed NAB alloy. The above results indicate that, among the three subregions of FSPed NAB alloy, subregion C containing stream-like  $\alpha$  colonies, finer  $\kappa_{iv}$ , and  $\beta'$  phases exhibits the best FCG resistance.

### C. Fatigue Crack Propagation Path

Figure 6 shows the fatigue crack profiles of various subregions in FSPed NAB alloy tested at the  $\Delta K$  value



of  $7 \text{ MPa}\sqrt{\text{m}}$ . At the subregion A (Figure 6(a)), the crack propagating through Widmanstätten  $\alpha$  or along the  $\alpha/\beta'$  phase boundaries (indicated by yellow arrows in Figure 6(a)) are observed. Fractured  $\beta'$  phase is also found, indicating that  $\beta'$  phase is more brittle than  $\alpha$  phase.<sup>[28]</sup> At subregion B (Figure 6(b)), the crack propagates through both  $\alpha$  colonies and  $\beta'$  phases. However, the crack prefers to propagate in a flat way in  $\beta'$  phase and more deflection in  $\alpha$  colonies (indicated by yellow arrows in Figure 6(b)). The crack propagation path of subregion C is similar with subregion B (indicated by yellow arrows in Figure 6(c)). Compared with FSPed region, the matrix alloy exhibits more deflection crack propagation path. It can clearly be observed from Figure 6(d) that the crack prefers to propagate along the  $\alpha/\kappa_{ii}$  interfaces and  $\kappa_{ii}$  can also change the crack propagation direction (indicated by yellow arrows in Figure 6(d)).

#### D. Microhardness

Figure 7 shows the microhardness distribution map of FSPed NAB alloy measured from the top surface to the bottom. Compared with the matrix alloy, all the subregions in FSPed NAB alloy have higher microhardness. Among the three subregions, the highest microhardness is obtained at subregion B (280 Hv). This is because the subregion has the highest content of  $\beta'$  phase (Figures 4(c) and (e)) and the  $\beta'$  phase has higher microhardness compared with the  $\alpha$  phase.<sup>[25]</sup> With further increasing the distance to matrix, the microhardness gradually decreases and the microhardness of matrix alloy is about 225 Hv.

## IV. DISCUSSION

### A. Effects of Microstructures on the FCGR of FSPed NAB Alloy

The above results indicate that the FSPed NAB alloy exhibits inhomogeneous microstructures at various

subregions. This is because various subregions in the FSPed NAB alloy experience different thermomechanical histories. This result has been reported in many investigations.<sup>[14,19]</sup> Here, we focus on the effect of microstructures on the FCGR of FSPed NAB alloy. Figure 8 shows the FCGR variations as a function of  $\Delta K$  at different subregions of FSPed NAB alloy. As can be seen, among the three subregions in FSPed NAB alloy, subregion A has the highest FCGR at various  $\Delta K$  values, followed by subregions B and C. In other words, the microstructures consisting of Widmanstätten  $\alpha$  and  $\beta'$  phases exhibit the highest FCGR, while the microstructures mainly including stream-like  $\alpha$  colonies and  $\beta'$  phase exhibit the lowest FCGR. This may be because Widmanstätten  $\alpha$  phase has lower Young's modulus compared with equiaxed  $\alpha$  phase,<sup>[26]</sup> while the FCGR of the material is proportional to  $(\Delta K/E)^4$ .<sup>[8]</sup> In other words, the material having the lower Young's modulus has higher FCGR. This may be one reason why subregions B and C have better fatigue crack growth resistance than subregion A. Compared with subregion C, subregion B has a higher FCGR. This may be attributed to the higher content of martensite  $\beta'$  phase in subregion B (Figure 4(c)). The  $\beta'$  phase is a metastable phase with a martensitic structure and has higher dislocation density and stored energy,<sup>[25]</sup> thereby accelerating the fatigue crack growth. It is also demonstrated by fatigue crack propagation path profile of FSPed NAB alloy that the martensite  $\beta'$  phase in subregion B prefers to propagate in a flat way (indicated by yellow arrows in Figure 6(b)). This is also consistent with our previous results that the heat-treated NAB alloy with a higher content of martensite  $\beta'$  phase has a higher FCGR.<sup>[27]</sup>

Figure 9 shows the EBSD maps of the fatigue crack paths at different subregions of FSPed NAB alloy tested at the  $\Delta K$  value of  $7.7 \text{ MPa}\sqrt{\text{m}}$ . Different colors in the figure represent the different orientation relations of  $\alpha$  grains. At subregion A (Figure 9(a)), both of the intergranular and transgranular crack propagation behaviors are observed (indicated by A, B, and C in

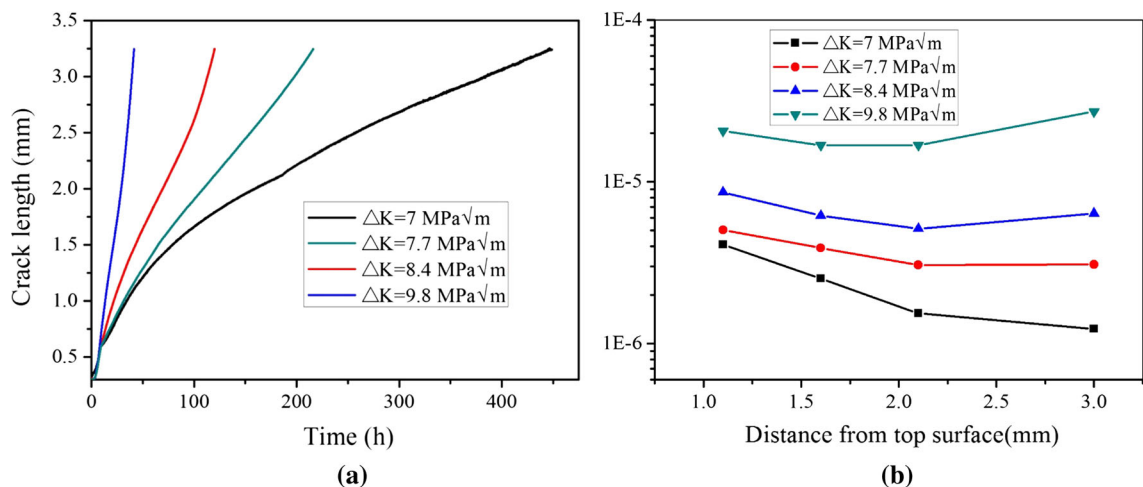


Fig. 5—Fatigue crack growth rates of FSPed NAB alloy at different stress intensity values ( $\Delta K$ ). (a) Crack length, a (mm), as a function of time (h). (b) Fatigue crack growth rates calculated from (a) in different subregions of FSPed NAB alloy.

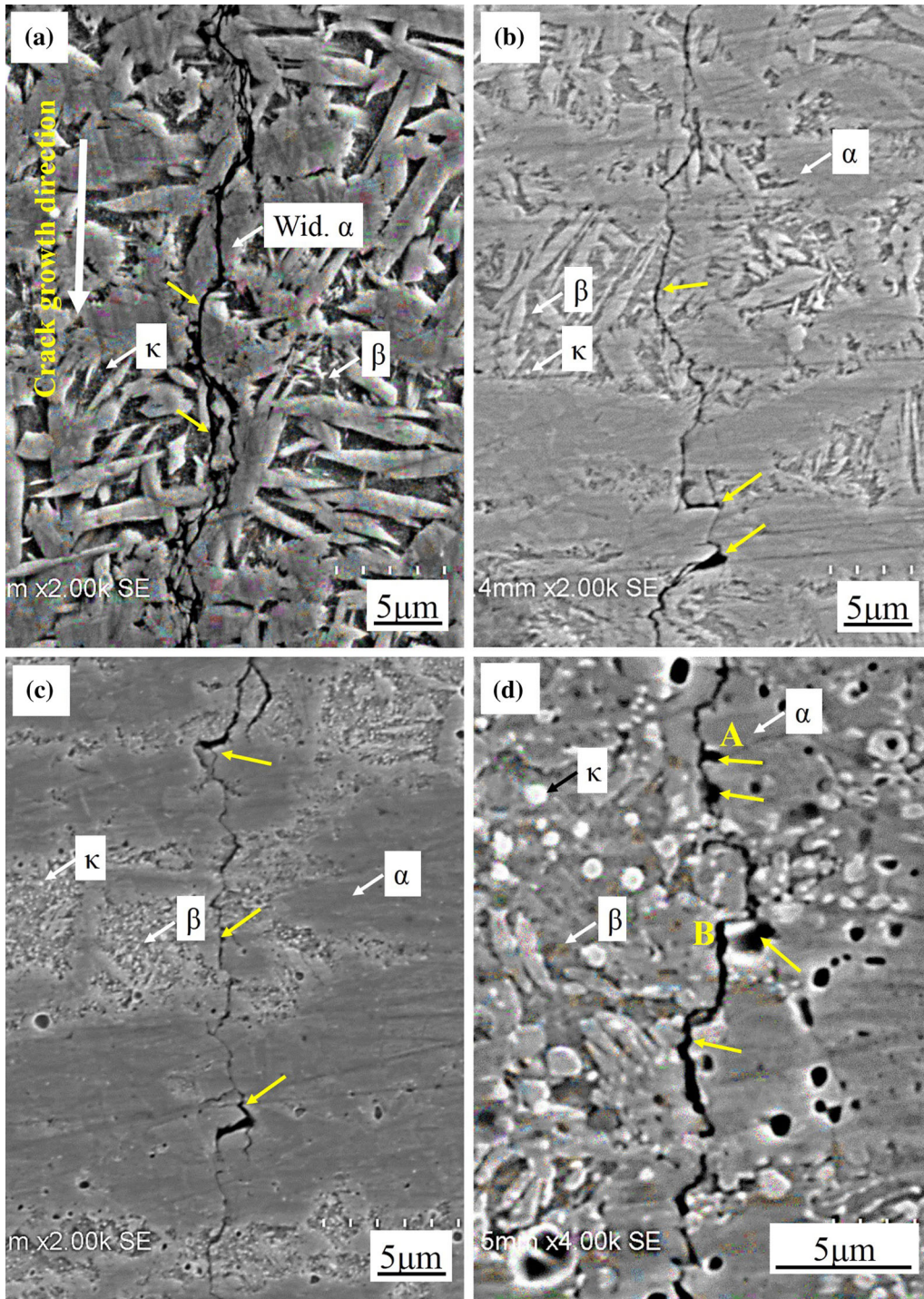


Fig. 6—Fatigue crack profiles at the stress intensity value ( $\Delta K$ ) of  $7 \text{ MPa}\sqrt{\text{m}}$  in various subregions of FSPed NAB alloy. (a), (b), (c) and (d) subregions A, B, and C and matrix, respectively.

Figure 9(a)). At subregions B and C, the crack propagates mainly along  $\alpha$  grain boundaries, although some transgranular crack propagation is also found (indicated by black arrows in Figures 9(b) and (c)). The boundary misorientation maps of various subregions in FSPed NAB reveal that most of  $\alpha$  gains have high-angle boundaries (above 40 deg), which indicate that the  $\alpha$  phase in the colonies experiences completely dynamic

recrystallization and forms equiaxed  $\alpha$  grains during FSP. Therefore, it is believed that, at low  $\Delta K$ , the crack tip plastic zone is small and  $\alpha$  grain boundaries can deflect the crack and increase the crack path tortuosity. Thus,  $\alpha$  phase can significantly decrease the FCGR at low  $\Delta K$ . As shown in Figures 4(c through f), subregion C has more  $\alpha$  phase than subregion B, which may be another reason for the lower FCGR of subregion C.



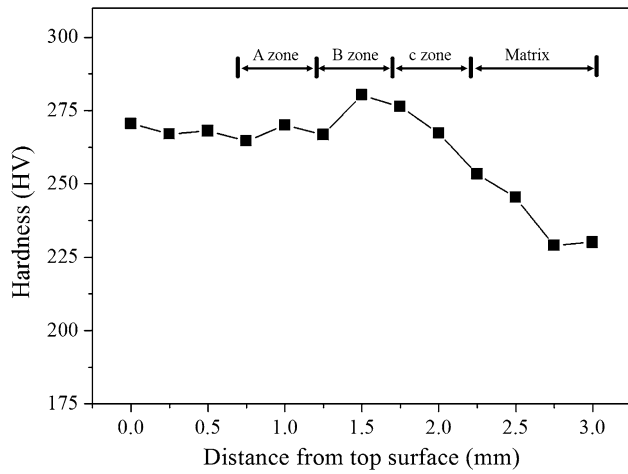


Fig. 7—Microhardness distribution profile obtained from the top surface to the bottom of FSPed NAB alloy.

Fine  $\kappa_{iv}$  phase is formed during FSP (see Figures 4(b), (d), and (f)), which has the Kurdjumov–Sachs or Nishiyama–Wasserman orientation relationship with the  $\alpha$  matrix.<sup>[28]</sup> These fine  $\kappa_{iv}$  phase can also deflect the crack tip or reduce damage accumulation of crack tip, thereby increasing the FCG resistance.<sup>[25]</sup> Our results are consistent with many previous investigations.<sup>[8,27]</sup> Borrego *et al.* studied the FCGR of age-hardened aluminum alloys and attributed the higher FCG resistance of the alloy to dispersed particles.<sup>[29]</sup> They considered that the dispersed particles promoted planar slip and crack deflection and increased the crack path tortuosity effect, thus decreasing FCGRs of the alloy.

### B. FCGR of Various Subregions in FSPed NAB Alloy

Based on the above results, various subregions of FSPed NAB alloy exhibit a large difference in FCGR at the  $\Delta K$  value of 7  $\text{MPa}\sqrt{\text{m}}$ , while the difference significantly decreases at the  $\Delta K$  value of 9.8  $\text{MPa}\sqrt{\text{m}}$  (Figures 5(b) and 8). In order to explain to this, the fracture surfaces for various subregions of FSPed NAB alloy are observed in detail, as shown in Figure 10. It can be found that FSPed NAB alloy tested at the  $\Delta K$  value of 7  $\text{MPa}\sqrt{\text{m}}$  has much more rough fatigue fracture surfaces on various subregions than that obtained at the  $\Delta K$  value of 9.8  $\text{MPa}\sqrt{\text{m}}$  (see yellow circle in Figures 10(a), (c), and (e)). It is indicated that  $\alpha$  grains can effectively deflect the fatigue crack at the  $\Delta K$  value of 7  $\text{MPa}\sqrt{\text{m}}$  and the deflection effect diminishes at the  $\Delta K$  value of 9.8  $\text{MPa}\sqrt{\text{m}}$ . This result is consistent with the observed fatigue crack path (shown in Figures 6 and 9, respectively). This is because, at low  $\Delta K$ , the crack tip plastic zone is small; in this situation, the crack deflection effect caused by the fine  $\alpha$  grains effectively decreases the FCGR of FSPed NAB alloy. With increasing  $\Delta K$ , the crack tip plastic zone significantly increases, leading to the disappearance of the aforementioned crack deflection effect. Thus, various subregions of the FSPed NAB alloy have a similar FCGR at the  $\Delta K$  value of 9.8  $\text{MPa}\sqrt{\text{m}}$ .<sup>[30,31]</sup>

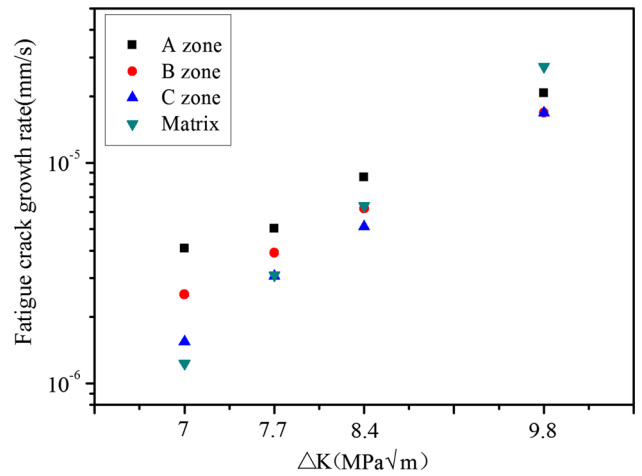


Fig. 8—Fatigue crack growth rates at different subregions of FSPed NAB alloy, which is calculated from Fig. 5(a).

### C. FCGR of FSPed Region Compared with Matrix Alloy

Based on the above analysis, the microstructures of forged NAB alloy are refined during FSP, increasing its microhardness significantly. It can be expected that FSPed NAB alloy has better FCG resistance. However, compared with matrix alloy, FSPed NAB alloy exhibits better FCG resistance only at higher  $\Delta K$  levels, while the matrix alloy has a lower FCGR at lower  $\Delta K$  levels (Figures 5(b) and 8). In order to understand the reason why matrix alloy has better FCG resistance at low  $\Delta K$  levels, the fracture surfaces of matrix alloy at the  $\Delta K$  values of 7 and 9.8  $\text{MPa}\sqrt{\text{m}}$  are observed, as shown in Figure 11. In Figure 11(a), large faceted surfaces of  $\alpha$  grains are observed (see red arrows in Figure 11(a)), indicating that the fracture mechanism of  $\alpha$  phase in matrix alloy is controlled by transgranular fracture mode at the  $\Delta K$  value of 7  $\text{MPa}\sqrt{\text{m}}$ , while the main fracture mechanism of  $\alpha$  phase in FSPed NAB alloy is intergranular fracture mode (see Figure 6). That may be one reason for the lower FCGR of matrix alloy that, generally, the alloy with the transgranular fracture has a lower FCGR than that with intergranular fracture.<sup>[8]</sup> Some  $\kappa_{ii}$  particles and voids with  $\kappa_{ii}$  morphologies are also observed in matrix alloy (see Figure 11(a)). The voids are formed when the  $\kappa_{ii}$  particles are pulled out of the matrix alloy during cyclic load. This result is consistent with the observed fatigue crack propagation path (see Figure 6(d)). It is indicated that the coarser  $\kappa_{ii}$  particles in the matrix can deflect the crack significantly, resulting in more rough fracture surface. Thus, coarser  $\kappa_{ii}$  particles can increase the FCG resistance of matrix alloy. While the coarser  $\kappa_{ii}$  particles are dissolved into the matrix alloy during FSP, fine  $\kappa_{iv}$  particles are precipitated during the following cooling (see Figure 4). The fine  $\kappa_{iv}$  particles can exert less influence on the fatigue crack growth resistance at low  $\Delta K$  compared with the coarser  $\kappa_{ii}$  particles. At the  $\Delta K$  value of 9.8  $\text{MPa}\sqrt{\text{m}}$ , a flat fracture surface is obtained (see Figure 11(b)), which indicates that the fatigue crack propagates in a flat way. In this situation, the deflection effect caused by

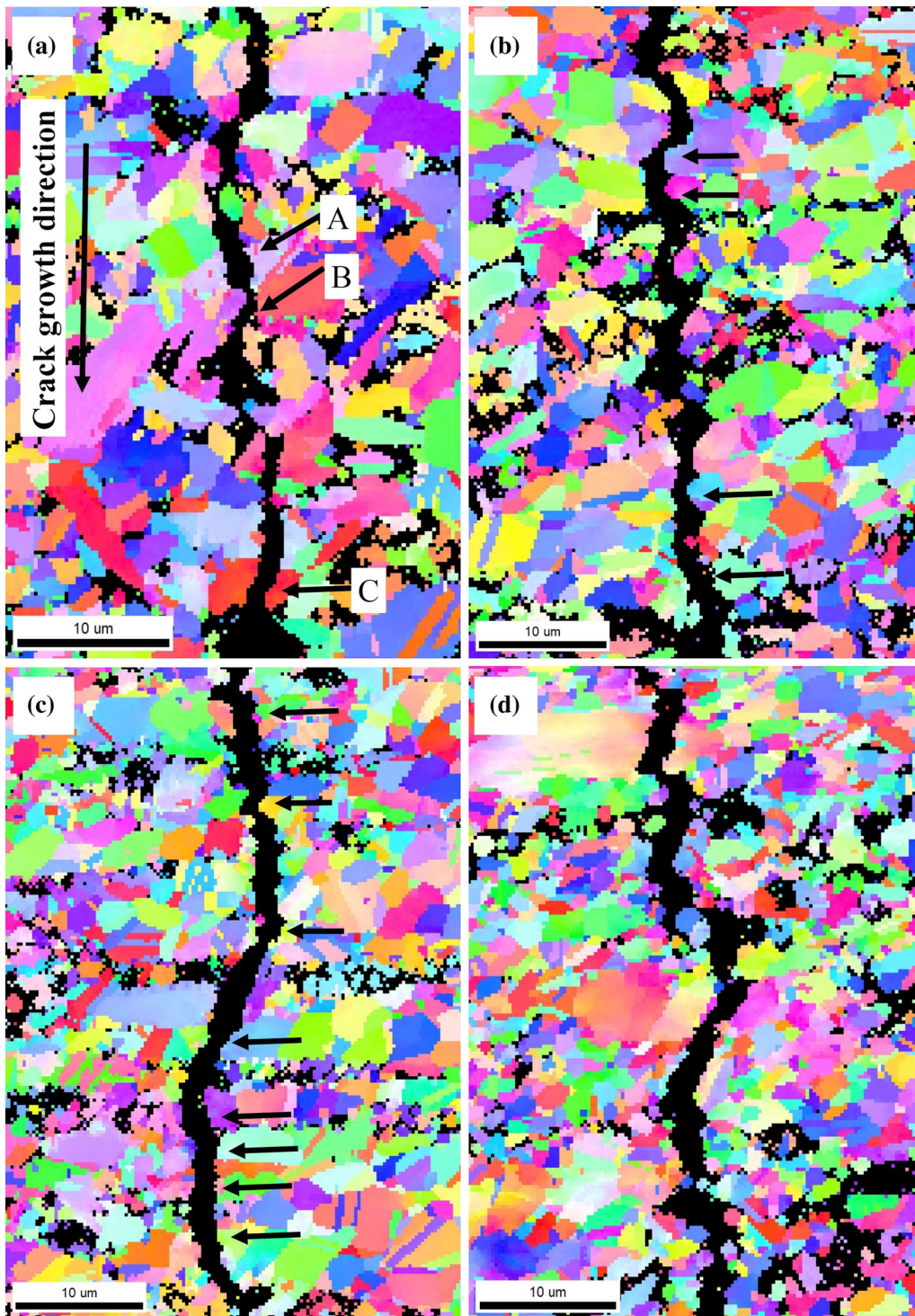


Fig. 9—EBSD maps of fatigue crack paths at different subregions of FSPed NAB alloy tested at the stress intensity value of  $7.7 \text{ MPa}\sqrt{\text{m}}$ . (a), (b), (c) and (d) Subregions A, B, and C and matrix, respectively.

microstructures has little influence on the FCGR of matrix alloy. It is reported that the fracture-related properties were controlled by the intrinsic fracture resistance, *i.e.*, mechanical properties and the tortuosity effect of the crack front.<sup>[31–33]</sup> At low  $\Delta K$  levels, the plastic zone of crack tip is small compared with grain size; in this situation, equiaxed  $\alpha$  grains and coarser  $\kappa_{ii}$  particles have

the ability to deflect main crack and the fracture mechanism is mainly controlled by the tortuosity effect of the crack front. At high  $\Delta K$  levels, the plastic zone of crack tip is large, and in this situation the mechanical properties play a main role in fatigue crack growth resistance. Thus, matrix alloy has a higher FCGR at the  $\Delta K$  value of  $9.8 \text{ MPa}\sqrt{\text{m}}$ .



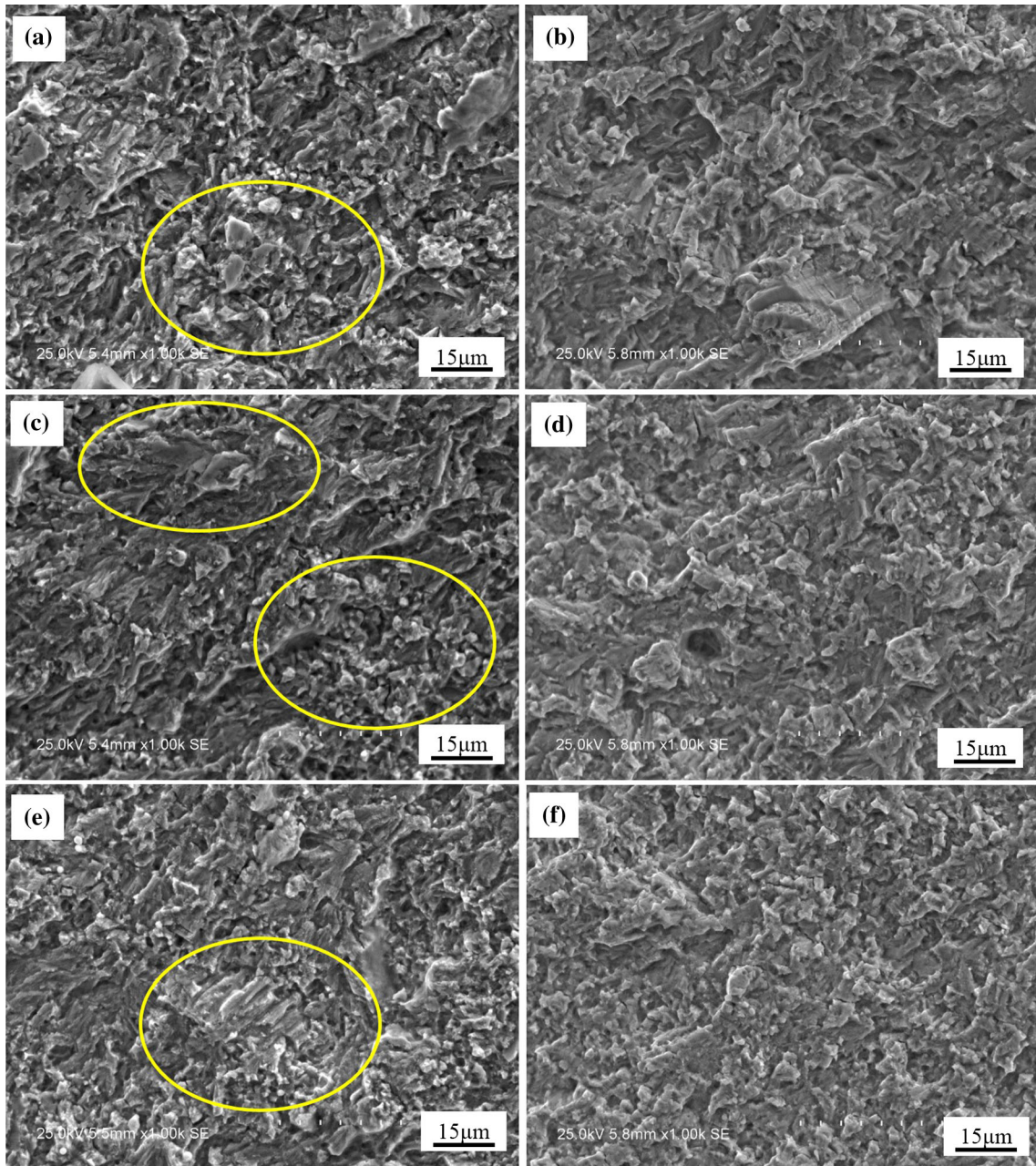


Fig. 10—Fatigue crack fracture surfaces of various subregions in FSPed NAB alloy at the  $\Delta K$  values of 7 and 9.8  $\text{MPa}\sqrt{\text{m}}$ . (a), (c) and (e) Subregions A, B, and C, respectively, at the  $\Delta K$  value of 7  $\text{MPa}\sqrt{\text{m}}$ . (b), (d) and (f) Region A, B, and C, respectively, at the  $\Delta K$  value of 9.8  $\text{MPa}\sqrt{\text{m}}$ .

Another important reason for the higher FCGR of FSPed NAB alloy may be the high content of  $\beta'$  phase formed during FSP due to high peak temperature. The  $\beta'$  phase is a metastable phase with a martensitic structure and has higher dislocation density and stored energy.<sup>[25]</sup> In some rich  $\beta'$  phase regions of FSPed NAB alloy, brittle crack can be formed (Figure 12), thereby significantly accelerating fatigue crack growth. In addition, high residual stress was also formed during FSP. Prevey *et al.* reported that the maximum residual stress of FSPed NAB alloy in the longitudinal (parallel to processing direction) and the transverse (normal to processing direction) directions was +200 and

−200 MPa, respectively.<sup>[34]</sup> Although the compressive stress in the transverse direction is beneficial to the FCG resistance of FSPed NAB alloy, however, it is reported that the longitudinal residual stresses were always higher than the transverse ones.<sup>[16]</sup> Thus, the high residual stress is also detrimental to the FCG resistance of FSPed NAB alloy.

Based on the above results, the fatigue crack growth behavior of FSPed NAB alloy at low and high  $\Delta K$  values can be summarized, as shown in Figure 13. At low  $\Delta K$  levels (Figure 13(a)), the crack tip plastic zone is small and the crack prefers to propagate along  $\alpha$  grain boundaries. Thus, the recrystallized  $\alpha$  grains in



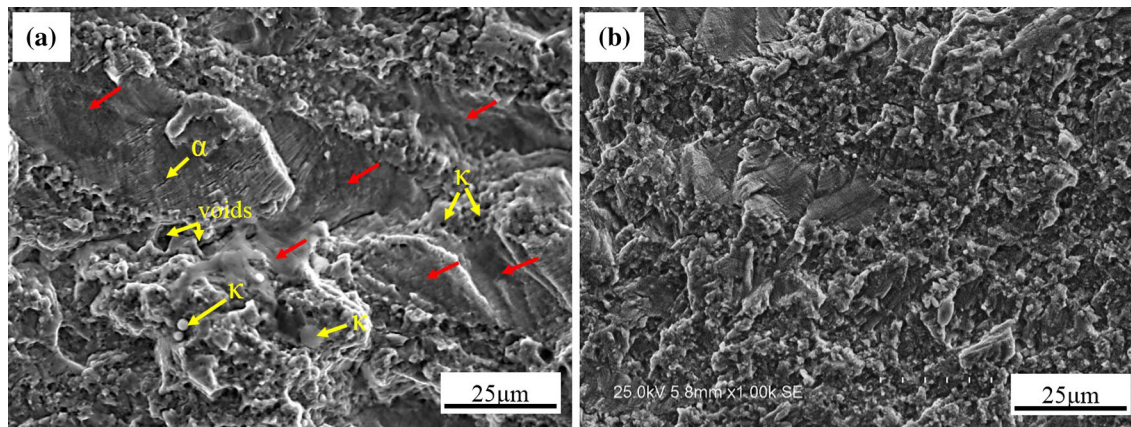


Fig. 11—Fracture surfaces of matrix alloy tested at different  $\Delta K$  values: (a)  $7 \text{ MPa}\sqrt{\text{m}}$  and (b)  $9.8 \text{ MPa}\sqrt{\text{m}}$ .

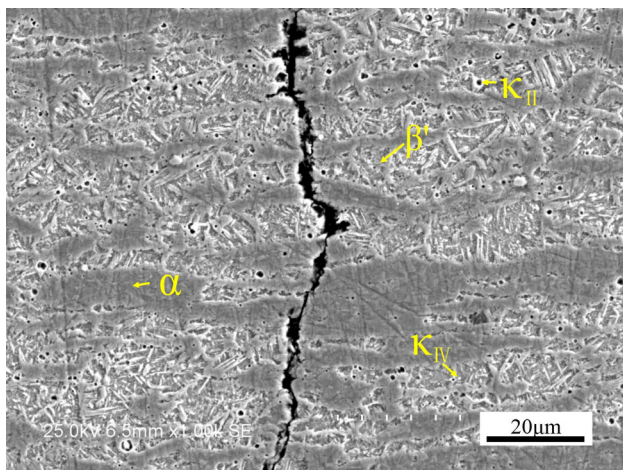


Fig. 12—Brittle crack obtained in rich  $\beta'$  phase subregion of FSPed NAB alloy.

subregions B and C significantly deflect the main crack, making a primary contribution to FCG resistance of FSPed NAB alloy, while the  $\beta'$  phase propagating in a flat way is detrimental to its FCG resistance. Coarser  $\kappa_{ii}$  particles in matrix exhibit more influence on the deflection effects of the main crack. This may be the reason why the matrix alloy has better FCG resistance at low  $\Delta K$  levels. At high  $\Delta K$  levels (Figure 13(b)), the crack tip plastic zone is large, and the deflection effect caused by microstructures diminishes. Thus, the main crack propagates in a flat way through all the subregions of FSPed and matrix alloy. In this situation, the mechanical properties of the alloy make a main contribution to the FCG resistance of the alloy. Therefore, the FSPed NAB alloy exhibits better FCG resistance compared with matrix alloy.

It should be noted that FSPed NAB alloy exhibits worse FCG resistance at low  $\Delta K$  levels compared to matrix alloy. A high content of  $\beta'$  phase produced during FSP is the main reason for the worse FCG resistance. In real production, the NAB alloy is heat treated at 948 K (675 °C) for 2 to 6 hours to eliminate

the  $\beta'$  phase.<sup>[22]</sup> In addition, the content of  $\beta'$  phase in FSPed NAB alloy can also be reduced by the decrease of heat input and the improvement of FSP tool is a good approach to decrease the heat input.<sup>[35]</sup> Therefore, in order to improve the FCGR of FSPed NAB alloy, post-heat treatment or the improvement of FSP tool will be tried in our future study.

## V. CONCLUSION

In this work, NiAl bronze (NAB) alloy was subjected to FSP. Inhomogeneous microstructures were formed in various subregions of FSPed NAB alloy. The effect of microstructures on the FCGR of FSPed NAB alloy was studied using DCPD method. The following conclusions can be drawn:

- (1) FSPed NAB alloy exhibits inhomogeneous microstructures from the top surface to the bottom that can be divided into three subregions: a subregion containing Widmanstätten  $\alpha$ , fine  $\kappa_{iv}$ , and  $\beta'$  phases, a subregion containing banded  $\alpha$  colonies, fine  $\kappa_{iv}$ , and  $\beta'$  phases, and a subregion containing stream-like  $\alpha$  colonies, fine  $\kappa_{iv}$ , and  $\beta'$  phases. During FSP,  $\alpha$  phase in the colonies experiences completely dynamic recrystallization and forms equiaxed  $\alpha$  grains.
- (2) The FCGR of FSPed NAB alloy continuously decreases from the top surface to the bottom. In the subregion with stream-like  $\alpha$  colonies, the alloy containing a higher content of equiaxed  $\alpha$  grains and fine  $\kappa_{iv}$  phase, and less retained  $\beta$  ( $\beta'$ ) phase exhibits the best FCG resistance. The equiaxed  $\alpha$  grains deflect the main crack and increase crack tortuosity effect, which make a main contribution to FCG resistance of FSPed NAB alloy, while the  $\beta'$  phase prefers to propagate in a flat way, which is detrimental to the FCG resistance of FSPed NAB alloy.
- (3) Compared to matrix alloy, FSPed NAB alloy exhibits better FCG resistance only at high  $\Delta K$  levels, while the matrix alloy has lower FCGR at low  $\Delta K$  levels. Fatigue crack growth resistance of



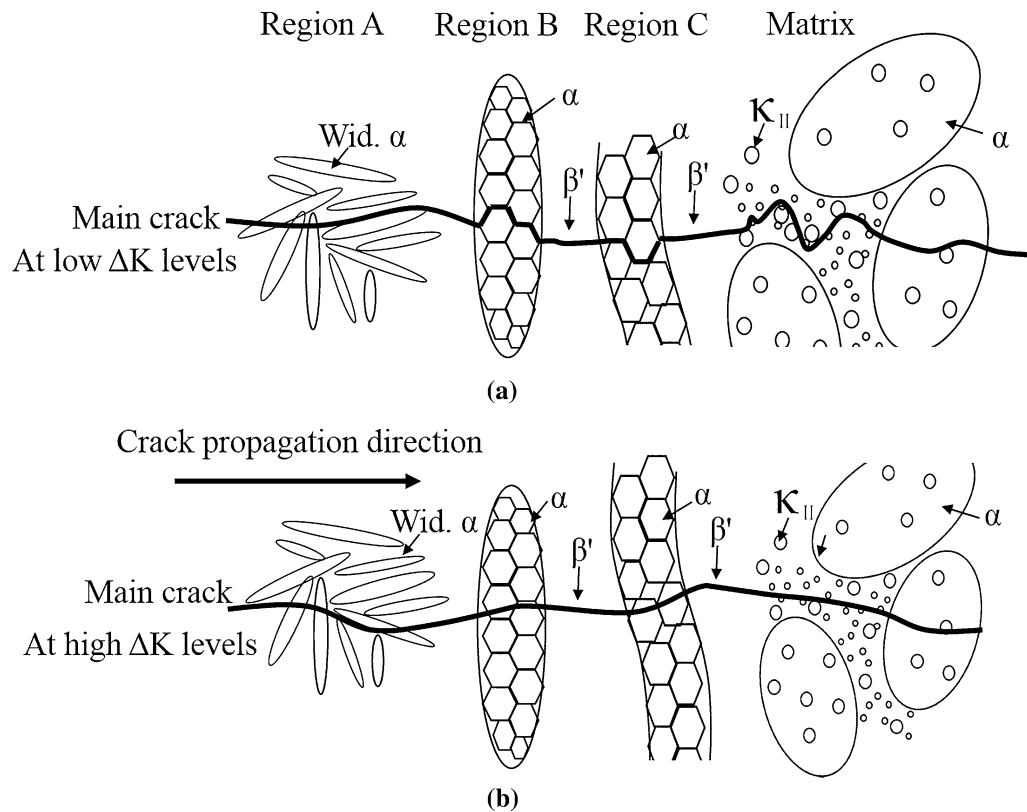


Fig. 13—Schematic diagram of crack propagation path in various subregions of FSPed NAB alloy and matrix at (a) low  $\Delta K$  levels and (b) high  $\Delta K$  levels.

FSPed NAB alloy is controlled by the mechanical properties and the tortuosity effect of the crack front. At low  $\Delta K$  levels, the fatigue crack deflection effect caused by coarser  $\kappa_{ii}$  particles in the matrix makes a main contribution to its better fatigue crack growth resistance. With increasing  $\Delta K$ , the aforementioned crack deflection effect gradually diminishes. In this situation, the mechanical properties play a main role in the FCG resistance, leading to higher FCGR of matrix alloy.

#### ACKNOWLEDGMENTS

Financial support for this research was jointly provided by 973 Program under Grant No. 2014CB046701, the National Science Foundation under Grant Nos. 51302168 and 51674167, the Shanghai Pujiang Program under Grant No. 15PJJD017, and the Science and Technology Planning Project of Jiujiang City.

#### REFERENCES

1. Z. Wu, Y.F. Cheng, L. Liu, W.J. Lv, and W.B. Hu: *Corros. Sci.*, 2015, vol. 98, pp. 260–70.
2. K. Oh-ishi and T.R. McNelley: *Metall. Mater. Trans. A.*, 2005, vol. 36A, pp. 1575–85.
3. D.R. Ni, B.L. Xiao, Z.Y. Ma, Y.X. Qiao, and Y.G. Zheng: *Corros. Sci.*, 2010, vol. 52 (5), pp. 1610–17.
4. A. Jahanafrooz, F. Hasan, G.W. Lorrmer, and N. Ridley: *Metall. Mater. Trans. A.*, 1982, vol. 34A, pp. 1951–56.
5. Q.N. Song, Y.G. Zheng, D.R. Ni, and Z.Y. Ma: *Corros. Sci.*, 2014, vol. 92, pp. 95–103.
6. X.Y. Xu, H. Wang, Y.T. Lv, W.J. Lu, and G.A. Sun: *Metall. Mater. Trans. A.*, 2016, vol. 47A (5), pp. 2081–92.
7. S. Fonlupt, B. Bayle, D. Delafosse, and J.L. Heuze: *Corros. Sci.*, 2005, vol. 47 (11), pp. 2792–2806.
8. X.Y. Xu, Y.T. Lv, M. Hu, D. Xiong, L.F. Zhang, L.Q. Wang, and W.J. Lu: *Int. J. Fatigue*, 2016, vol. 82, pp. 579–87.
9. A. Chakrabarti, A. Sarkar, T. Saravanan, A. Nagesha, R. Sandhya, and T. Jayakumar: *Proc. Eng.*, 2014, vol. 86, pp. 103–10.
10. Z.B. Qin, Z. Wu, X.S. Zen, Q. Luo, L. Liu, W.J. Lu, and W.B. Hu: *Corrosion*, 2016, vol. 72 (10), pp. 1269–80.
11. C.H. Tang, F.T. Cheng, and H.C. Man: *Surf. Coat. Tech.*, 2004, vol. 182, pp. 300–07.
12. C.H. Tang, F.T. Cheng, and H.C. Man: *Mater. Sci. Eng. A*, 2004, vol. 373, pp. 195–203.
13. J.Q. Su, S. Swaminathan, S.K. Menon, and T.R. McNelley: *Metall. Mater. Trans. A*, 2011, vol. 42a (8), pp. 2420–30.
14. K. Oh-ishi and T.R. McNelley: *Metall. Mater. Trans. A*, 2004, vol. 35A, pp. 2951–60.
15. S. Hanke, A. Fischer, M. Beyer, and J.D. Santos: *Wear*, 2011, vol. 273 (1), pp. 32–37.
16. R.S. Mishra and Z.Y. Ma: *Mater. Sci. Eng. R*, 2005, vol. 50 (1–2), pp. 1–78.
17. W.A. Palko, R.S. Fielder, and P.F. Young: *Mater. Sci. Forum*, 2003, vols. 426–432, pp. 2909–14.
18. D.R. Ni, P. Xue, and Z.Y. Ma: *Metall. Mater. Trans. A*, 2011, vol. 42 (8), pp. 2125–35.
19. D.R. Ni, P. Xue, D. Wang, B.L. Xiao, and Z.Y. Ma: *Mater. Sci. Eng. A*, 2009, vol. 524 (1–2), pp. 119–28.
20. S. Swaminathan, K. Oh-Ishi, A.P. Zhilyaev, C.B. Fuller, B. London, M.W. Mahoney, and T.R. McNelley: *Metall. Mater. Trans. A*, 2009, vol. 1A (3), pp. 631–40.
21. R. Nandan, T. Debroy, and H. Bhadeshia: *Prog. Mater. Sci.*, 2008, vol. 53 (6), pp. 980–1023.

22. Y.T. Lv, L.Q. Wang, X.Y. Xu, and W.J. Lu: *Metals*, 2015, vol. 5 (3), pp. 1695–1703.
23. Y.T. Lv, L.Q. Wang, Y.F. Han, X.Y. Xu, and W.J. Lu: *Mater. Sci. Eng. A*, 2015, vol. 643, pp. 17–24.
24. Y.T. Lv, L.Q. Wang, X.Y. Xu, Y.F. Han, and W.J. Lu: *Mater. Trans.*, 2015, vol. 56 (9), pp. 1523–29.
25. Y.L. Wang, Q.L. Pan, L.L. Wei, B. Li, and Y. Wang: *Mater. Des.*, 2014, vol. 55, pp. 857–63.
26. J.Z. Dong, F.G. Li, and C.P. Wang: *Mater. Sci. Eng. A*, 2013, vol. 580, pp. 105–13.
27. Y.T. Lv, M. Hu, L.Q. Wang, X.Y. Xu, Y.F. Han, and W.J. Lu: *J. Mater. Res.*, 2015, vol. 30 (20), pp. 3041–48.
28. A.J.F. Hansan, G.W. Lorimer, and N. Ridley: *Metall. Mater. Trans A*, 1982, vol. 13A, pp. 1337–45.
29. L.P. Borrego, J.M. Costa, S. Silva, and J.M. Ferreira: *Int. J. Fatigue*, 2004, vol. 26 (12), pp. 1321–31.
30. X.H. Shi, W.D. Zeng, C.L. Shi, H.J. Wang, and Z.Q. Jia: *Mater. Sci. Eng. A*, 2015, vol. 621, pp. 252–58.
31. X.H. Shi, W.D. Zeng, C.L. Shi, H.J. Wang, and Z.Q. Jia: *Mater. Sci. Eng. A*, 2015, vol. 621, pp. 143–48.
32. G. Lütjering, J. Albrecht, C. Sauer, and T. Krull: *Mater. Sci. Eng. A*, 2007, vols. 468–470, pp. 201–09.
33. X.H. Shi, W.D. Zeng, S.K. Xue, and Z.Q. Jia: *J. Alloy. Compd.*, 2015, vol. 631, pp. 340–49.
34. P.S. Prevey, D.J. Hornbach, and D.N. Jayaraman: *Mater. Sci. Forum*, 2007, vols. 539–543, pp. 3807–13.
35. J. Yang, B.L. Xiao, D. Wang, and Z.Y. Ma: *Mater. Sci. Eng. A*, 2010, vol. 527, pp. 708–14.